

# Giant Electric Energy Density in Epitaxial Lead-Free Thin Films with Coexistence of Ferroelectrics and Antiferroelectrics

Biaolin Peng, Qi Zhang, Xing Li, Tieyu Sun, Huiqing Fan, Shanming Ke, Mao Ye, Yu Wang, Wei Lu, Hanben Niu, James F. Scott, Xierong Zeng\*, Haitao Huang\*

Dr. Biaolin Peng, Xing Li, Dr. Tieyu Sun, Prof. Yu Wang, Dr. Wei Lu, Prof. Haitao Huang  
Department of Applied Physics, The Hong Kong Polytechnic University, Kowloon, Hong Kong, China  
E-mail: aphhuang@polyu.edu.hk

Dr. Biaolin Peng, Dr. Shanming Ke, Dr. Mao Ye, Prof. Xierong Zeng  
Shenzhen Key Laboratory of Special Functional Materials, Shenzhen Engineering Laboratory for Advanced Technology of Ceramics, College of Materials Science and Engineering, Shenzhen University, Shenzhen 518060, PR China.  
E-mail: zengxier@szu.edu.cn

Dr. Biaolin Peng, Prof. Hanben Niu  
Key Laboratory of Optoelectronic Devices and Systems of Ministry of Education and Guangdong Province, College of Optoelectronic Engineering, Shenzhen University, Shenzhen, 518060, China.

Prof. Qi Zhang  
Department of Manufacturing and Materials, Cranfield University, Cranfield, Bedfordshire, MK43 0AL, United Kingdom  
State Key Laboratory of Advanced Technology for Materials Synthesis and Processing, Wuhan University of Technology, Wuhan 430070, Hubei, PR China

Prof. Huiqing Fan  
State Key Laboratory of Solidification Processing School of Materials Science and Engineering, Northwestern Polytechnical University, Xi'an 710072, China

Prof. James F. Scott  
Cavendish Laboratory, University of Cambridge, Cambridge, CB3 0HE, United Kingdom

Keywords: energy storage, relaxor, antiferroelectric, PLD, MPB

Ferroelectrics/antiferroelectrics with high dielectric breakdown strength have the potential to store a great amount of electrical energy, attractive for many modern applications in electronic devices and systems. Here we demonstrate that a giant electric energy density ( $154 \text{ J}\cdot\text{cm}^{-3}$ , 3 times the highest value of lead-based systems and 5 times the value of the best dielectric/ferroelectric polymer), together with the excellent fatigue-free property, good

thermal stability and high efficiency, is realized in pulsed laser deposited  $(\text{Bi}_{1/2}\text{Na}_{1/2})_{0.9118}\text{La}_{0.02}\text{Ba}_{0.0582}(\text{Ti}_{0.97}\text{Zr}_{0.03})\text{O}_3$  (BNLBTZ) epitaxial lead-free relaxor thin films with the coexistence of ferroelectric (FE) and antiferroelectric (AFE) phases. This is endowed by high epitaxial quality, great relaxor dispersion and the coexistence of the FE/AFE phases near the morphotropic phase boundary (MPB). The giant energy storage effect of the BNLBTZ lead-free relaxor thin films may make a great impact on the modern energy storage technology.

## 1. Introduction

In recent years, there has been an increasing interest to develop new dielectric capacitors that possess high power density, fast charge/discharge ( $< 1 \mu\text{s}$ ), low cost and high thermal and mechanical stability.<sup>[1-3]</sup> These capacitors could find applications in defibrillators, detonators, and power electronics, etc., that require high power density.<sup>[1-3]</sup> However, compared with fuel cells, Li-ion batteries and supercapacitors, the dielectric capacitors have the lowest energy density.<sup>[4, 5]</sup> To improve this, much attention has been particularly paid to antiferroelectric ceramics such as PZ,<sup>[6, 7]</sup> PLZT,<sup>[8, 9]</sup> PZN-PMN-PT,<sup>[4]</sup> and PLZST,<sup>[4]</sup> etc., since they normally have higher energy density than ferroelectric and paraelectric ceramics at comparable electric field.<sup>[2]</sup>

The energy density in bulk ceramics is usually less than  $1 \text{ Jcm}^{-3}$  because of the limitation of low dielectric breakdown strength ( $< 100 \text{ kVcm}^{-1}$ ).<sup>[10]</sup> With the development of high-quality thin films by sol-gel, pulsed laser deposition (PLD), and molecular beam epitaxy (MBE), etc., large energy density, mainly in lead-based antiferroelectric thin films has been achieved due to the higher dielectric breakdown strength ( $> 500 \text{ kVcm}^{-1}$ ).<sup>[3, 8, 11, 12]</sup> For example, a high energy density of  $53 \text{ Jcm}^{-3}$  at  $3500 \text{ kVcm}^{-1}$  was obtained in relaxor antiferroelectric  $(\text{Pb}_{0.92}\text{La}_{0.08})(\text{Zr}_{0.9}\text{Ti}_{0.05})\text{O}_3$  sol-gel thin film.<sup>[8]</sup> However, widespread applications of lead-based materials are prohibited due to the toxicity of lead. As a lead-free dielectric material, poly(vinylidene fluoride) (PVDF)-based polymer was also widely studied and a high energy

density of  $27 \text{ Jcm}^{-3}$  at  $8000 \text{ kVcm}^{-1}$  was reported.<sup>[1,4]</sup> However, its lifetime and reliability are seriously impaired at the maximum operating temperature (typically less than  $85 \text{ }^\circ\text{C}$ ), seriously limiting its applications as capacitors.

In this study,  $(\text{Bi}_{1/2}\text{Na}_{1/2})_{0.9118}\text{La}_{0.02}\text{Ba}_{0.0582}(\text{Ti}_{0.97}\text{Zr}_{0.03})\text{O}_3$  (BNLBTZ) epitaxial lead-free relaxor thin films with a coexistence of rhombohedral ferroelectric (FE) and tetragonal antiferroelectric (AFE) phases were deposited by PLD method on (001) single crystal  $\text{SrTiO}_3$  substrates. The film composition was exquisitely designed to be near the morphotropic phase boundary (MPB) of the  $(1-x)(\text{Bi}_{1/2}\text{Na}_{1/2})\text{Ti}-x\text{BaTiO}_3$  (BNT-BT) solid solution, as shown in **Figure 1**.<sup>[13]</sup> An appropriate content of La doping is to reduce the Curie temperature of the MPB composition  $0.94(\text{Bi}_{1/2}\text{Na}_{1/2})\text{Ti}-0.06\text{BaTiO}_3$ , improve the degree of relaxor dispersion and maintain a certain amount of antiferroelectric phase. A small amount of Zr doping is to further gently adjust the Curie temperature. The deposited thin films have high saturation polarizations, low remnant polarizations and slim  $P$ - $E$  hysteresis loops, resulting in giant electric energy densities of  $131 \text{ Jcm}^{-3}$  (efficiency  $\sim 95\%$ ) and  $154 \text{ Jcm}^{-3}$  (efficiency  $\sim 97\%$ ) at  $3500 \text{ kVcm}^{-1}$  in (100)- and (111)-oriented thin films, respectively.

## 2. Results and discussions

### 2.1. Structure

**Figure 2a** compares the XRD patterns of the BNLBTZ thin film (deposited by PLD) and the bulk ceramic target (synthesized by a sol-gel route). The BNLBTZ thin film exhibits a pure perovskite phase with preferential (100) orientation and a perfect epitaxial feature to the  $\text{La}_{0.7}\text{Sr}_{0.3}\text{MnO}_3$  (LSMO) bottom electrode because of the small lattice mismatch ( $a_{\text{LSMO}} = 3.85 \text{ \AA}$  and  $a_{\text{BNLBTZ}} = 3.91 \text{ \AA}$ ). The rocking curve (inset of Fig. 2a) of the (200) peak, whose full width at half maximum is less than  $0.03^\circ$ , indicates a highly single crystalline preferential growth orientation. The  $\Phi$  scan of (110) (tilted about  $45^\circ$  away from the (100)) (inset of Fig. 2a) further reveals a good 4-fold rotational symmetry of the BNLBTZ epitaxial thin film. The

slight deviation of the peak separation away from the theoretical value of  $90^\circ$  indicates that the BNLBTZ thin film possesses a pseudo cubic structure.

The cross-sectional SEM image of the (100)-oriented BNLBTZ thin film (Supporting Information Figure S1) shows clearly the epitaxial BNLBTZ film (thickness  $\sim 350$  nm), the bottom  $\text{La}_{0.7}\text{Sr}_{0.3}\text{MnO}_3$  (LSMO) electrode (thickness  $\sim 80$  nm), and the  $\text{SrTiO}_3$  substrate. The LSMO/STO and LSMO/BNLBTZ interfaces are all uniform and smooth, and no obvious grain boundaries can be detected, indicating a good epitaxial growth. Atomic force microscope (AFM) micrograph shows that (100) oriented BNLBTZ thin film has a low average surface roughness ( $R_a \sim 6.3$  nm and  $R_b \sim 7.9$  nm) (Supporting Information Figure S2), a feature of good epitaxial growth.<sup>[14]</sup> A direct evidence of the good epitaxial growth can be observed from the high resolution transmission electron microscope (HRTEM) image (Figure 2b) of the interface between the BNLBTZ thin film and the LSMO bottom electrode, where the selected area electron diffraction (SAED) shows the same set of pattern for both the film and the bottom electrode.

The cross-sectional TEM image of the (100)-oriented BNLBTZ thin film (Figure 2c) shows laminar AFE nanodomains (indicated by black arrows in Figure 2c). The SAED pattern along pseudo-cubic [013] zone axis (inset of Figure 2d) shows bright  $1/2\{ooo\}$  ( $o$ : odd Miller indices) and weak  $1/2\{oeo\}$  ( $e$ : even Miller indices) superlattice reflections, corresponding to a large portion of rhombohedral FE and a small portion of tetragonal AFE phases, respectively.<sup>[15]</sup> Streaking of the superlattice reflection can be observed along the [001] direction. It is believed that the doping of La on the A-site of the  $\text{ABO}_3$  perovskite structure disrupted the long range ordering of the AFE phase and led to the observed incommensurate modulations of the AFE phase.<sup>[16]</sup> The piezo-response force microscopy (PFM) vertical phase image (upper-right corner inset of Figure 2c) shows that the FE/AFE nanodomains can grow up into larger ones under the stimulus of an appropriate electric field.

## 2.2. Dielectric properties

**Figure 3** shows the temperature dependence of the relative dielectric permittivity ( $\varepsilon(T)$ ) and the dielectric loss ( $\tan \delta(T)$ ) of BNLBTZ bulk ceramic and (100)-oriented thin film. The dielectric permittivity ( $\varepsilon_{10\text{kHz}, 300\text{K}}=1897$ ) of the thin film at room temperature is much higher than that ( $\varepsilon_{10\text{kHz}, 300\text{K}}=1618$ ) of the bulk. However, the dielectric permittivity ( $\varepsilon_{10\text{kHz}, 300\text{K}}=1255$ ; Supporting Information Figure S3) of the (111)-oriented BNLBTZ thin film is far below that of the bulk, implying that the rhombohedral phase is the dominant phase instead of the tetragonal one (consistent with the TEM result in Fig. 2d) since for a rhombohedral phase the dielectric permittivity along the [111] direction is less than that along the [100] direction.<sup>[17]</sup> In the bulk BNLBTZ, two dielectric permittivity maxima (at 10 kHz) can be observed at  $T_{m1}=374$  K and  $T_{m2}=562$  K, which correspond to the phase transition temperatures of  $T_{\text{FE-AFE}}$  and  $T_{\text{AFE-PE}}$ , respectively. By contrast, for the (100)-oriented BNLBTZ epitaxial thin film, the two dielectric permittivity maxima were smeared due to the relaxor dispersion in the thin film, especially near  $T_{m1}$ . The relaxor dispersion degree around  $T_{m1}$  can be estimated by the Lorentz-type relation,<sup>[18]</sup>  $\varepsilon_A/\varepsilon=1+(T-T_A)^2/2(\delta_A)^2$ , where  $T_A$  ( $T_A \neq T_{m1}$ ) and  $\varepsilon_A$  are the temperature of the dielectric permittivity peak and the extrapolated value of  $\varepsilon$  at  $T = T_A$ , respectively. The parameter  $\delta_A$  reflects the relaxor diffuseness of the dielectric peak. The greater the relaxor dispersion is, the larger the  $\delta_A$  is. The Lorentz fitting parameters  $\delta_A$  around  $T_{m1}$  for the bulk and the thin film (the red dash dotted line in Figure 3) are 74 and 150, respectively, indicating a much higher degree of the relaxor dispersion in thin films, which can be attributed to small size effect, substrate constraint, interface charge and other defects (such as vacancies).<sup>[19, 20]</sup>

Furthermore, the two dielectric permittivity maxima of the epitaxial thin film are both less than those of the bulk. One moves to the low temperature side of  $T_{m1}$  and the other to the high temperature side of  $T_{m2}$ , leading to a wider temperature range of the AFE phase and a lower temperature coefficient of permittivity/capacitance (650-850 ppmK<sup>-1</sup>) from room temperature up to 473 K.

Due to the greater relaxor dispersion in the thin film, the dielectric loss ( $\tan \delta(T)$ ) of the (100) oriented BNLBTZ thin film is much higher than that of the BNLBTZ bulk ceramic in the entire temperature range measured.

Previous research results showed that the re-orientation of polar nanoclusters in relaxor FE/AFE phase plays a very important role in the electric field dependence of the dielectric permittivity, in addition to the contribution from intrinsic lattice phonon polarization.<sup>[21]</sup> The room temperature dielectric permittivity ( $\varepsilon(E)$ ) and the loss ( $\tan \delta(E)$ ) at 10 kHz exhibit a nonlinear dependence on the bias electric field (inset of Fig. 3). Dielectric tunability and figure-of-merit (*FOM*) are defined as:  $(\varepsilon(0)-\varepsilon(E))/\varepsilon(0)$ , and  $\text{tunability}/\tan\delta$ , respectively.<sup>[20]</sup> They both increase with increasing electric field, and a tunability of 87% and an *FOM* of 12 are achieved at  $E=750 \text{ kVcm}^{-1}$ , very promising for the application in dielectric tunable devices. The  $\varepsilon(E)$  of the (100)-oriented BNLBTZ relaxor thin film can be described by the following equation.<sup>[21]</sup>

$$\varepsilon(E) = \varepsilon_r(0) / \{1 + \lambda[\varepsilon_0 \varepsilon_r(0)^3 E^2]\}^{1/3} + (P_r x / \varepsilon_0) [\cosh(Ex)]^{-2}, \quad x = P_r L^3 / (2k_B T) \quad (1)$$

where  $\varepsilon_0$  is the vacuum permittivity,  $\lambda$  a temperature-independent coefficient,  $\varepsilon_r(0)$  the relative dielectric permittivity at zero field,  $P_r$  the polarization of a polar nanocluster,  $L$  the cluster size (or correlation length),  $k_B$  the Boltzmann's constant and  $T$  the temperature. The first term in Eq. (1) represents the polarization contribution from lattice phonons, and the second stands for the re-orientation contribution from polar nanoclusters. The black solid line (inset of Figure 3) fitted according to Eq. (1) agrees quite well with the experimental data. Obviously, the nanoclusters make a significant contribution to  $\varepsilon$  below  $\sim 200 \text{ kVcm}^{-1}$ , which decreases quickly with increasing  $E$  and almost disappears at an electric field above  $300 \text{ kVcm}^{-1}$ . It can also be seen (inset of Figure 3) that the dielectric permittivity contributed by the nanoclusters ( $\varepsilon_{cluster}$ ) is 1322 under zero bias, about 70% of the total dielectric permittivity ( $\varepsilon_{total}$ ). The size of nanoclusters, according to the fitting, is  $L = 3.9 \text{ nm}$ .

### 2.3. Energy storage

The energy density ( $W$ ) of a dielectric-based compound is given by

$$W = \int_{P_r}^{P_{\max}} E dP, \quad 0 \leq E \leq E_{\max}; \quad (2)$$

where  $E$  is the applied electric field that causes the variation in electric polarization  $P$ ,  $P_r$  is the remnant polarization, and  $P_{\max}$  is the maximum polarization under the applied field. It is obvious that, to have a high energy density  $W$ , the material should have a high  $P_{\max}$  and a low  $P_r$ . They are realized in the BNLBTZ films through the coexistence of relaxor FE and AFE phases, where the relaxor FE phase helps maintain a high  $P_{\max}$  and both the relaxor FE and AFE phases keep a low  $P_r$ . From the  $P$ - $E$  hysteresis loop of the (100)-oriented thin film (**Figure 4**) it can be seen that the  $P_{\max}$  and  $P_r$  are 72.1 and 4.03  $\mu\text{Ccm}^{-2}$ , respectively and the breakdown field exceeds 2180  $\text{kVcm}^{-1}$  (Fig. 4). A careful examination on the  $P$ - $E$  loop shows that it is not an FE-type single loop since four peaks can be observed in the corresponding  $I$ - $E$  curve (inset of Fig. 4). The four peaks occur at a relatively low electric field of 125  $\text{kVcm}^{-1}$  and are indicative of a relaxor AFE nature of the epitaxial thin film. One may argue that double hysteresis loops are not necessarily indicative of antiferroelectricity. As originally shown by Merz,<sup>[22]</sup> double loops also occur for first-order FE transitions over a temperature range of a few degrees above  $T_c$ , where the applied field induces spontaneous polarization. In  $\text{BaTiO}_3$  this occurs over a temperature range from the Curie temperature  $T_c$  to  $T_c+11\text{K}$ . However, this can be ruled out in the present case because there is no evidence for such a temperature dependence. One may also propose that double hysteresis loops may be due to the aging of point defects.<sup>[23]</sup> This can also be ruled out since the double hysteresis loops were observed in our fresh samples without aging. By integrating the discharging portion of the  $P$ - $E$  loop according to Eq. (2), an energy density of 43.89  $\text{Jcm}^{-3}$  at 2180  $\text{kVcm}^{-1}$  can be achieved on the (100)-oriented thin film, which is approximately 44 times that of the bulk BNLBTZ ( $\sim 1 \text{ Jcm}^{-3}$  at 103  $\text{kVcm}^{-1}$ ), as illustrated by the shaded area in Supporting Information Figure

S4). The energy density of  $43.89 \text{ Jcm}^{-3}$  achieved in this lead-free material is comparable to the best lead-containing PLZT at similar electric fields. It can be further improved by changing the epitaxial growth orientation from (100) to (111), where an energy density of  $54.3 \text{ Jcm}^{-3}$  was achieved (Fig. 4). The good quality of the (111)-oriented epitaxial film can be reflected from the XRD pattern, the rocking curve of (111) and the *phi* scan of (110) (Supporting Information Figure S5). The higher energy density of the (111)-oriented film can be ascribed to the higher  $P_{\max}$  ( $82.5 \mu\text{Ccm}^{-2}$ ) along [111] which is the spontaneous polarization direction for a system with a dominant rhombohedral phase.

In real applications, capacitor efficiency ( $\eta$ ) is also an important factor to consider, which is defined as the ratio of the discharging (output) energy to the charging (input) energy,

$$\eta = W / (W + W_{\text{Loss}}); \quad (3)$$

where  $W_{\text{loss}}$  is the energy loss density, equivalent to the integrated area the closed  $P$ - $E$  hysteresis loops. At an electric field of  $2180 \text{ kVcm}^{-1}$ , the energy loss densities of the (100)- and (111)-oriented BNLBTZ thin films are  $9.2$  and  $10.3 \text{ Jcm}^{-3}$ , respectively, which result in efficiencies of  $79$  and  $81\%$ , respectively.

For energy storage applications, cycling life is another important factor to consider. An electrochemical supercapacitor can normally withstand a cycling number of  $10^5$ . In this study, after  $10^8$  fatigue cycles (bi-polar cycling), a relatively high  $P_{\max}$  ( $70.5 \mu\text{Ccm}^{-2}$ ) and a low  $P_r$  ( $2.94 \mu\text{Ccm}^{-2}$ ) can still be maintained for (100)-oriented BNLBTZ thin film under an electric field of  $2180 \text{ kVcm}^{-1}$  (Figure 4), with a corresponding high energy density of  $37.94 \text{ Jcm}^{-3}$ . Since, in real applications, dielectric capacitors normally undergo unipolar cycling, it is thus believed that the cycling number of our thin film capacitor can be well above  $10^8$ . The excellent anti-fatigue property of our epitaxial thin film is resulted from (1) the use of a highly conductive  $p$ -type oxide  $\text{La}_{0.7}\text{Sr}_{0.3}\text{MnO}_3$  as the bottom electrode,<sup>[24]</sup> and (2) the great relaxor dispersion and the unique nanodomain structure near MPB (Figures 2c and 2d) that help



reduce the large strain associated to the AFE-FE phase transition under an applied electric field, similar to the case in irradiated relaxor P(VDF-TrFE) copolymer network.<sup>[25]</sup>

In addition to the above, thermal stability should also be considered in real capacitor applications.<sup>[3]</sup> The *P-E* loops of the (100)-oriented thin film at selected temperatures after  $10^8$  fatigue cycles are shown in Supporting Information Figure S6. From the inset (b) of Figure 4, it can be seen that the variations of the energy density and the efficiency are below 2.6 and 5%, respectively, from room temperature up to 110 °C. The slight increase in energy density as the temperature is increased from room temperature to 100°C is due to the increased leakage current at higher temperatures, where the *P-E* loop becomes more and more leaky (Supporting Information Figure S6). It is noted that the temperature for the maximum energy density (black arrow in the inset (b) of Figure 4) is close to  $T_{m1}$  (red arrow in Figure 3) of the bulk BNLBTZ, not that of the (100)-oriented thin film. One possible reason is that the applied electric field tends to turn the AFE phase into an FE one, resulting in enhanced FE-AFE transition temperature  $T_{m1}$  of this epitaxial thin film.

According to Eq. (2), a higher energy density can be achieved if the thin film can withstand a higher electric field. With the help of an external voltage amplifier (ferroelectric tester Precision Premier II) and to simulate the condition in a real application, a unipolar voltage pulse was used to charge the thin film capacitor. The resulting *P-E* loops of the (100)- and (111)-oriented BNLBTZ epitaxial thin films (**Figure 5**) show that both of them can withstand a very high electric field, up to  $3500 \text{ kVcm}^{-1}$ . Extremely high  $P_{\text{max}}$  has been achieved ( $90.55 \text{ } \mu\text{Ccm}^{-2}$  in (100) film and  $113.45 \text{ } \mu\text{Ccm}^{-2}$  in (111) one). As a result, giant energy storage effect have been observed in (100) and (111) films, with  $W=131$  and  $154 \text{ Jcm}^{-3}$ , respectively. The efficiencies are 95% and 97%, respectively, comparable to the Columbic efficiency of a good electrochemical supercapacitor.<sup>[26]</sup> Further increasing the electric field will cause a failure of the top electrode (inset (b) of Figure 5) due to the large leakage current at the beginning of charging (inset (a) of Figure 5). The leakage current measurement

(Supporting Information Figure S7) shows that, under a high electric field, the conduction in (100) thin film satisfies a bulk-limited conduction mechanism, following a Poole-Frenkel relation.<sup>[27]</sup> It is believed that the flat film/electrode interface (Figure 2b and Supporting Information Figure S1) is one of the reasons to achieve a high breakdown field. An even higher energy density is achievable if the film quality can be further improved and the top electrode can be optimized by using, for example, a LaNiO<sub>3</sub> electrode.<sup>[11]</sup> The utilization of a ‘dead layer’ at the film/electrode interface could be another way to further increase the energy density, especially for a large area device.<sup>[28]</sup>

To benchmark the capability of the BNLBTZ thin films for applications in energy storage devices, the energy densities of the BNLBTZ thin films in the present work are compared with a number of promising materials previously reported (**Figure 6** and Supporting Information Table S1). The energy densities in both the (100)- and (111)-oriented BNLBTZ thin films reported here are significantly better than previously reported lead-based (PZ, PLZT, PZN-PMN-PT, and PLZST, etc.) and lead-free materials (PVDF and BFST, etc.).<sup>[1, 3, 4, 6-9, 12]</sup> By implementing a multilayer configuration, the BNLBTZ reported in this work will be a very promising, environmentally friendly, inexpensive (compared with scandium-based),<sup>[29]</sup> and thermally stable (compared with polymers) capacitor material for potential applications in electric energy storage, due to its ultrahigh energy density ( $154 \text{ Jcm}^{-3}$   $\sim 7.7 \text{ Whkg}^{-1}$ ) and ultrahigh power density ( $2.6 \times 10^8 \text{ Wkg}^{-1}$ ) (inset of Figure 6).

### 3. Conclusions

In conclusion, a giant energy storage effect ( $137$  and  $154 \text{ Jcm}^{-3}$  for (100)- and (111)-oriented thin films, respectively) with high efficiency, excellent anti-fatigue property ( $10^8$  cycles) and thermal stability (variation below 2.6% at  $2180 \text{ kVcm}^{-1}$  from room temperature to  $110 \text{ }^\circ\text{C}$ ) has been achieved in the lead-free relaxor BNLBTZ epitaxial thin films. This is accomplished by the high epitaxial quality, great relaxor dispersion and the coexistence of FE/AFE phase near the morphotropic phase boundary. The giant energy storage density of the

thin film with lead-free, fast charge/discharge, low cost, high thermal stability, may make it a promising material for modern energy storage technology, especially in electronic and electric systems.

#### 4. Experimental procedure

##### ***Fabrication of BNLBTZ target:***

BNLBTZ target was fabricated by sol-gel and conventional solid-state reaction methods.  $\text{Bi}(\text{OAc})_3$ ,  $\text{Na}(\text{OAc})$ ,  $\text{La}(\text{NO}_3)_3$  and  $\text{Ba}(\text{CH}_3\text{COO})_2$  were dissolved in glacial acetic, 2-methoxyethanol and deionized water. In order to compensate the Bi and Na loss during sintering, 20% excess Bi and Na were added. Separately, acetylacetone and 2-methoxyethanol were added to a mixture of  $\text{Zr}(\text{O}^n\text{Pr})_4$  and Titanium-4-butoxide, and the resulting solution was stirred for 30 min at room temperature. The Bi/Na/La/Ba and Zr/Ti solutions were then mixed and stirred for 1 h at room temperature. After aging for 24 h, the BNLBTZ sol was air-dried. The natural dried gel was pyrolyzed at 350 °C for 30 min and then fired at 600 °C for 30 min, and finally calcined at 900 °C for 2 h in air in a tube furnace. After grinding for 2 h in an agate mortar, the calcined powders were then compacted into pellets with 20 mm in diameter and 3 mm in thickness under a 300 MPa cold isostatic pressing and were sintered at 1150 °C for 6 h in air, and then cooled to room temperature at a furnace cooling rate.

##### ***Fabrication of BNLBTZ thin films:***

The as-prepared BNLBTZ target exhibited a prominent pure perovskite crystalline phase in the XRD pattern (Figure 2). The BNLBTZ thin film was grown by pulsed laser deposition (PLD) using a KrF laser excimer ( $\lambda = 248$  nm) with pulse repetition rate of 5 Hz. A 80-nm-thick lattice matched  $\text{La}_{0.7}\text{Sr}_{0.3}\text{MnO}_3$  (LSMO) thin film was deposited as the bottom electrode between the BNLBTZ film and the  $\text{SrTiO}_3$  (STO) substrate. The BNLBTZ/LSMO bilayers were deposited *in situ* at the substrate temperature of 700 °C, oxygen pressure of 30 Pa and laser pulse energy density of  $5 \text{ Jcm}^{-2}$ . After the deposition, the bilayer films were post-annealed *in situ* at the deposition temperature under an oxygen pressure of 400 Pa for 20 min

before they were cooled to room temperature to minimize oxygen vacancies. The aforementioned PLD processing parameters and the corresponding plasma image for depositing BNLBTZ thin films are briefly summarized in Supporting Information Table S2. The final thickness of the BNLBTZ film was about 350 nm. Circular Cr/Au top electrodes with about 100  $\mu\text{m}$  in diameter were deposited by RF magnetron sputtering using a shadow mask.

### ***Characterization:***

The crystallinity of the BNLBTZ film was monitored by X-ray diffraction (XRD, Rigaku 9 KW Smartlab, Japan) on a diffractometer, using Cu K $\alpha$  radiation ( $\lambda = 1.5406 \text{ \AA}$ ). The cross-sectional morphology of the film was examined by scanning electron microscope (SEM, FEI Sirion 200). The microstructure of the film was studied by transmission electron microscopy (TEM; JEOL JEM-2100F). The out-of-plane feature of the ferroic domains in the film was investigated by scanning probe microscope (SPM; Bruker Multimode 8). Dielectric permittivity measurements were carried out using an impedance analyzer (4294A, Agilent) with a perturbation voltage  $V_{\text{ac}} = 500 \text{ mV}$ . The polarization-electric field ( $P$ - $E$ ) hysteresis loop and leakage current ( $I$ - $E$ ) were obtained by means of a ferroelectric tester (Precision Premier II, Radiant Technologies Inc.). All samples were measured with top-and-bottom electrode configuration. The temperature of the sample was controlled via feedback from a thermocouple in contact with the sample, with an accuracy of 0.1°C.

### **Supporting Information**

Supporting Information is available from the Wiley Online Library or from the author.

### **Acknowledgements**

This work was supported by the Hong Kong Polytechnic University (Project Nos.: A-PL54, G-UC69 and 1-ZVCG), the National Natural Science Foundation of China (51402196, 51272161, 51172187), the China Postdoctoral Science Foundation (006858), and the

Shenzhen Science and Technology Research Foundation (CXB201005240010A), 111  
Program (B08040) of MOE.

Received: ((will be filled in by the editorial staff))  
Revised: ((will be filled in by the editorial staff))  
Published online: ((will be filled in by the editorial staff))

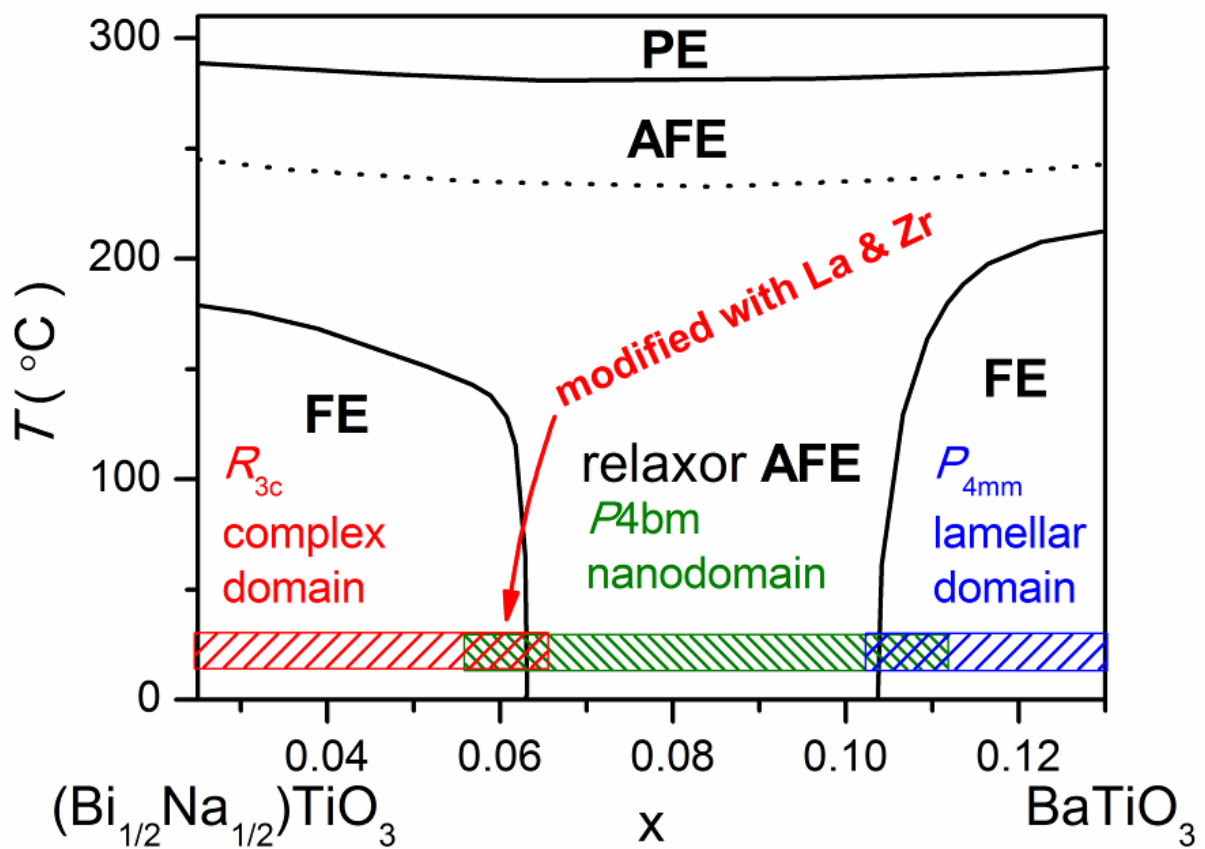
- [1] B. J. Chu, X. Zhou, K. L. Ren, B. Neese, M. R. Lin, Q. Wang, F. Bauer, Q. M. Zhang, *Science* **2006**, *313*, 334.
- [2] S. Kwon, W. Hackenberger, E. Alberta, E. Furman, M. Lanagan, *IEEE Electr. Insul. Mag.* **2011**, *27*, 43.
- [3] T. M. Correia, M. McMillen, M. K. Rokosz, P. M. Weaver, J. M. Gregg, G. Viola, M. G. Cain, G. L. Brennecka, *J. Am. Ceram. Soc.* **2013**, *96*, 2699.
- [4] K. Yao, S. Chen, M. Rahimabady, M. S. Mirshekarloo, S. Yu, F. E. H. Tay, T. Sritharan, L. Lu, *Ieee Transactions on Ultrasonics Ferroelectrics and Frequency Control* **2011**, *58*, 1968.
- [5] a) N. S. Choi, Z. Chen, S. A. Freunberger, X. Ji, Y. K. Sun, K. Amine, G. Yushin, L. F. Nazar, J. Cho, P. G. Bruce, *Angew Chem Int Ed Engl* **2012**, *51*, 9994. b) M. S. Whittingham, *MRS Bull.* **2008**, *33*, 411.
- [6] M. Ye, Q. Sun, X. Chen, Z. Jiang, F. Wang, R. Whatmore, *J. Am. Ceram. Soc.* **2011**, *94*, 3234.
- [7] A. K. Tagantsev, K. Vaideeswaran, S. B. Vakhrushev, A. V. Filimonov, R. G. Burkovsky, A. Shaganov, D. Andronikova, A. I. Rudskoy, A. Q. Baron, H. Uchiyama, D. Chernyshov, A. Bosak, Z. Ujma, K. Roleder, A. Majchrowski, J. H. Ko, N. Setter, *Nat. Commun.* **2013**, *4*, 2229.

- [8] B. Ma, D.-K. Kwon, M. Narayanan, U. Balachandran, *J. Mater. Res.* **2011**, *24*, 2993.
- [9] B. Ma, M. Narayanan, U. Balachandran, *Mater. Lett.* **2009**, *63*, 1353.
- [10] a) X. Li, Z. Xi, W. Long, P. Fang, *Chin. Sci. Bull.* **2013**, *58*, 2893. b) F. Gao, X. Dong, C. Mao, W. Liu, H. Zhang, L. Yang, F. Cao, G. Wang, J. Jones, *J. Am. Ceram. Soc.* **2011**, *94*, 4382.
- [11] J. Ge, X. Dong, Y. Chen, F. Cao, G. Wang, *Appl. Phys. Lett.* **2013**, *102*, 142905.
- [12] X. Hao, J. Zhou, S. An, *J. Am. Ceram. Soc.* **2011**, *94*, 1647.
- [13] C. Ma, X. Tan, *Solid State Commun.* **2010**, *150*, 1497.
- [14] S. K. Pandey, A. R. James, R. Raman, S. N. Chatterjee, A. Goyal, C. Prakash, T. C. Goel, *Physica B* **2005**, *369*, 135.
- [15] L. A. Schmitt, M. Hinterstein, H.-J. Kleebe, H. Fuess, *J. Appl. Crystallogr.* **2010**, *43*, 805.
- [16] Z. Xu, X. H. Dai, D. Viehland, *Physical Review B* 1995, *51*, 6261; H. He, X. Tan, *Physical Review B* **2005**, *72*.
- [17] Y. L. Li, L. E. Cross, L. Q. Chen, *J. Appl. Phys.* **2005**, *98*, 064101.
- [18] S. Ke, H. Fan, H. Huang, H. L. W. Chan, *Appl. Phys. Lett.* **2008**, *93*.
- [19] a) J. H. Haeni, P. Irvin, W. Chang, R. Uecker, P. Reiche, Y. L. Li, S. Choudhury, W. Tian, M. E. Hawley, B. Craigo, A. K. Tagantsev, X. Q. Pan, S. K. Streiffer, L. Q. Chen, S. W. Kirchoefer, J. Levy, D. G. Schlom, *Nature* **2004**, *430*, 758. b) B. L. Peng, H. Q. Fan, Q. Zhang, *Adv. Funct. Mater.* **2013**, *23*, 2987.
- [20] T. M. Correia, Q. Zhang, *J. Appl. Phys.* **2010**, *108*, 044107.
- [21] C. Ang, Z. Yu, *Physical Review B* **2004**, *69*.
- [22] W. Merz, *Physical Review* **1953**, *91*, 513.
- [23] X. Ren, *Nat Mater* **2004**, *3*, 91.
- [24] F. Chen, Q. Z. Liu, H. F. Wang, F. H. Zhang, W. Wu, *Appl. Phys. Lett.* **2007**, *90*, 192907.
- [25] Q. M. Zhang, V. Bharti, X. Zhao, *Science* **1998**, *280*, 2101.
- [26] K. Xie, J. Li, Y. Lai, Z. a. Zhang, Y. Liu, G. Zhang, H. Huang, *Nanoscale* **2011**, *3*, 2202.

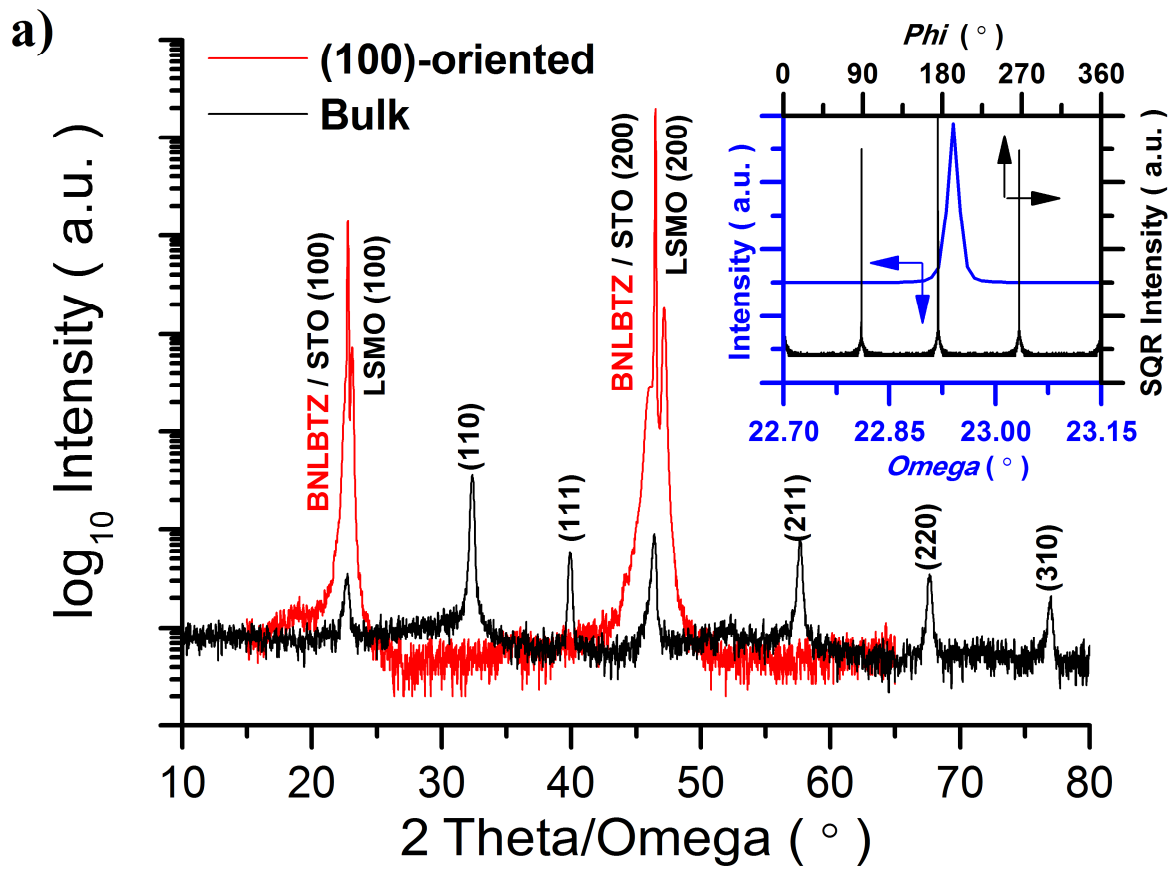
[27] F.-C. Chiu, J.-J. Wang, J. Y.-m. Lee, S. C. Wu, *J. Appl. Phys.* **1997**, *81*, 6911.

[28] M. McMillen, A. M. Douglas, T. M. Correia, P. M. Weaver, M. G. Cain, J. M. Gregg, *Appl. Phys. Lett.* **2012**, *101*, 242909.

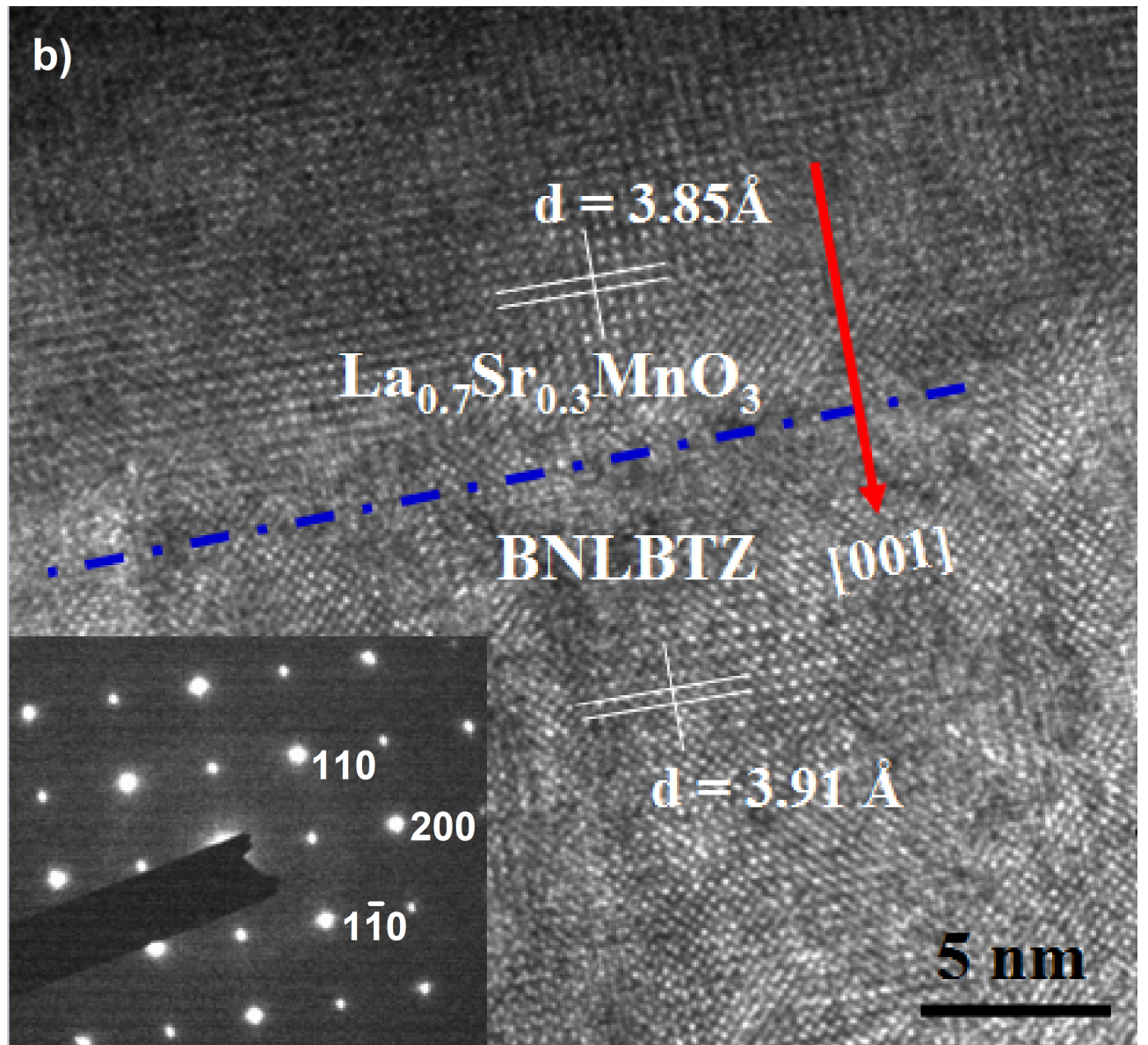
[29] H. Ogihara, C. A. Randall, S. Trolier-McKinstry, *J. Am. Ceram. Soc.* **2009**, *92*, 1719.

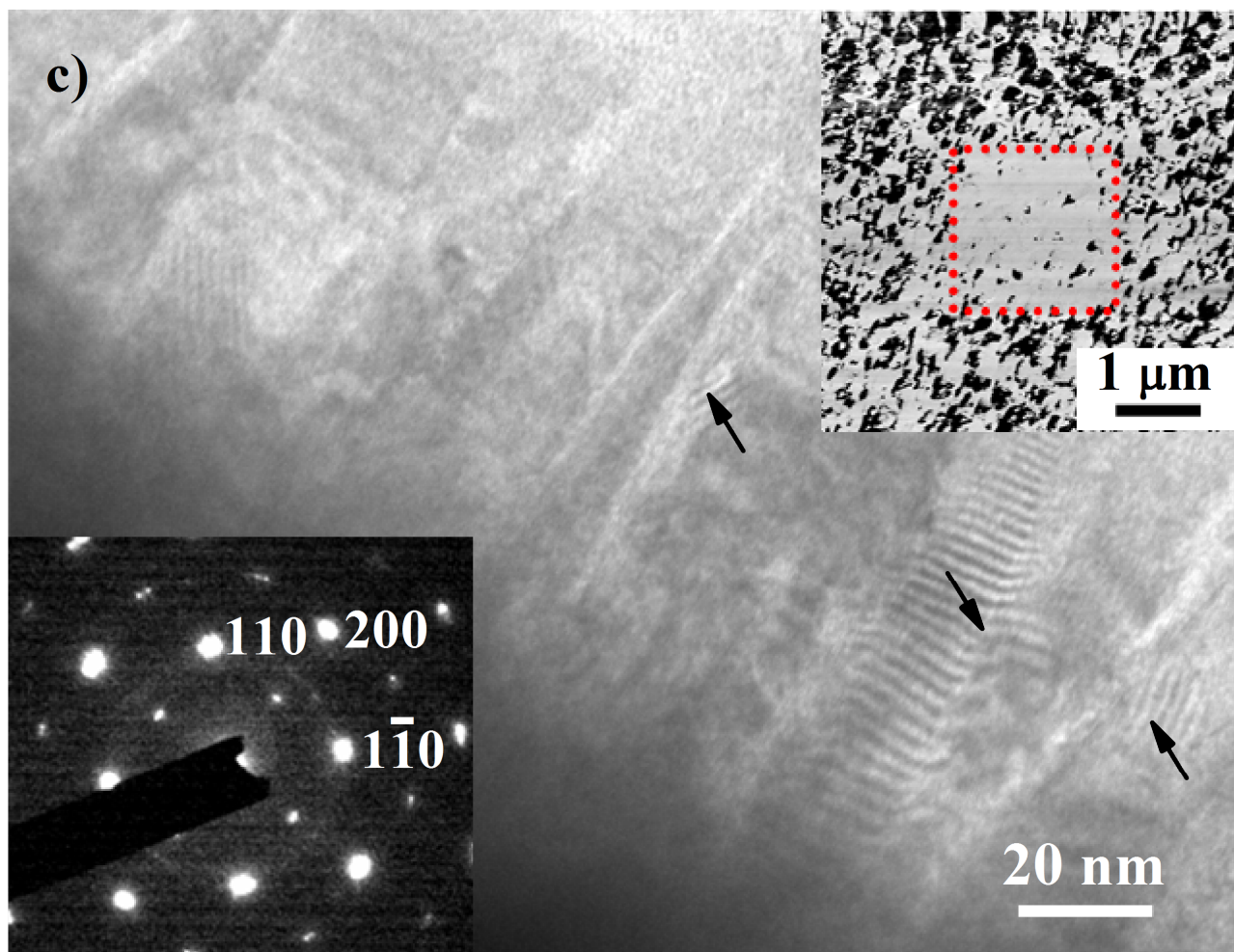


**Figure 1.** The phase diagram of the  $(1-x)(\text{Bi}_{1/2}\text{Na}_{1/2})\text{Ti}-x\text{BaTiO}_3$  solid solution. PE, AFE and FE represent paraelectric, antiferroelectric, and ferroelectric phases, respectively<sup>[13]</sup>.









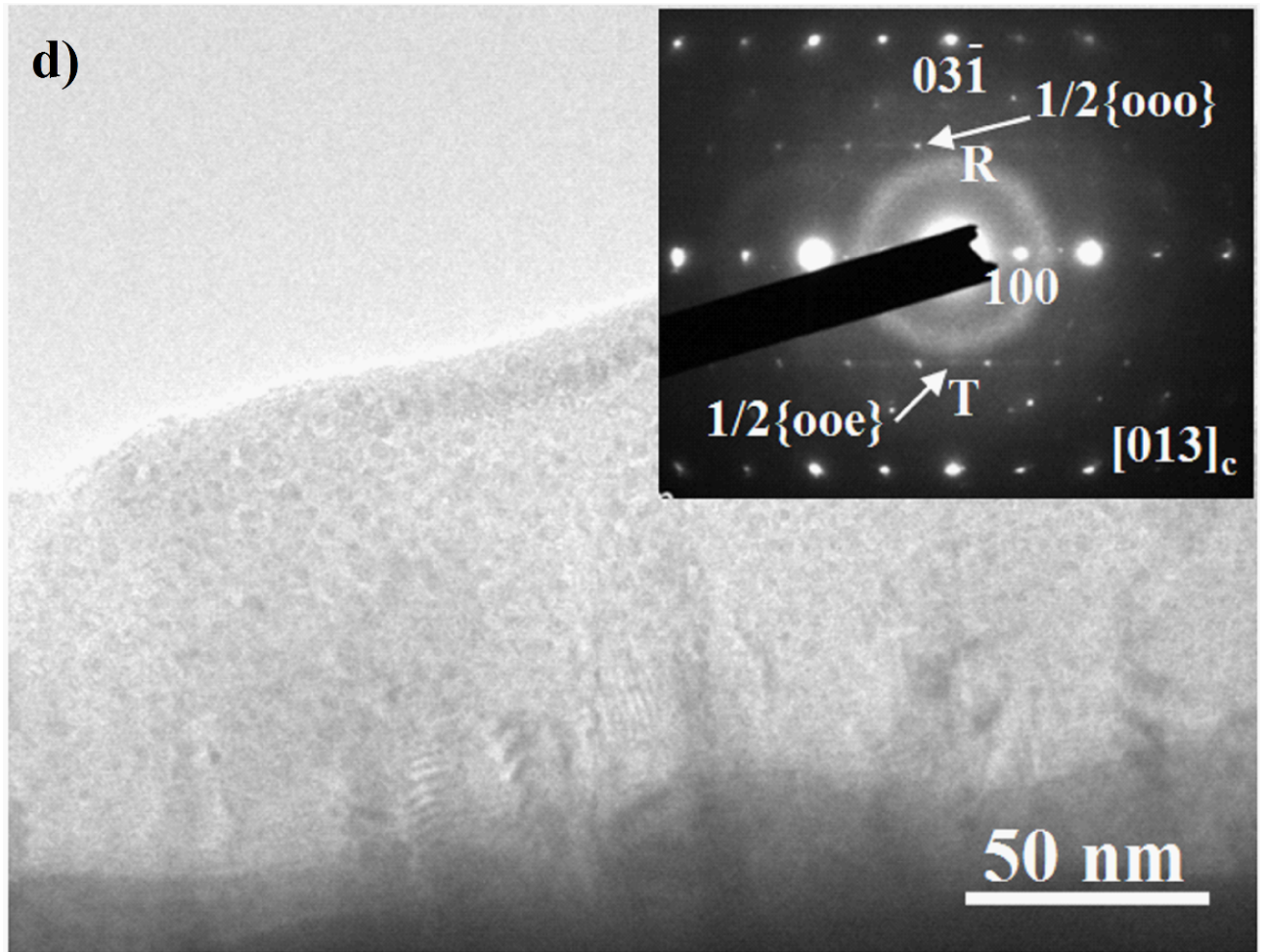


**Figure 2.** XRD patterns and cross-sectional TEM images of the (100)-oriented BNLBTZ thin film. (a) XRD pattern of the BNLBTZ bulk and thin film (the diffraction intensity is expressed in a logarithmic scale). Inset: the rocking curve of (200) and the  $\Phi$  scanning of (110). (b) Cross-sectional HRTEM image of the interface between BNLBTZ epitaxial thin film and  $\text{La}_{0.7}\text{Sr}_{0.3}\text{MnO}_3$  bottom electrode. The inset is the SAED pattern on a large area containing both the film and the substrate. (c) TEM image. Lower-left corner inset: SAED pattern along [001] zone axis. Upper-right corner inset: PFM vertical phase image (red square section and peripheral area represent a single domain under 10 V dc bias and nanodomains under 0 V dc bias, respectively). (d) TEM image. Inset: SAED pattern along [013] zone axis. Arrows indicate the  $1/2\{ooo\}$  and  $1/2\{ooe\}$  superstructure reflections, where R means rhombohedral and T tetragonal, and  $o$  denotes odd Miller index and  $e$  even.

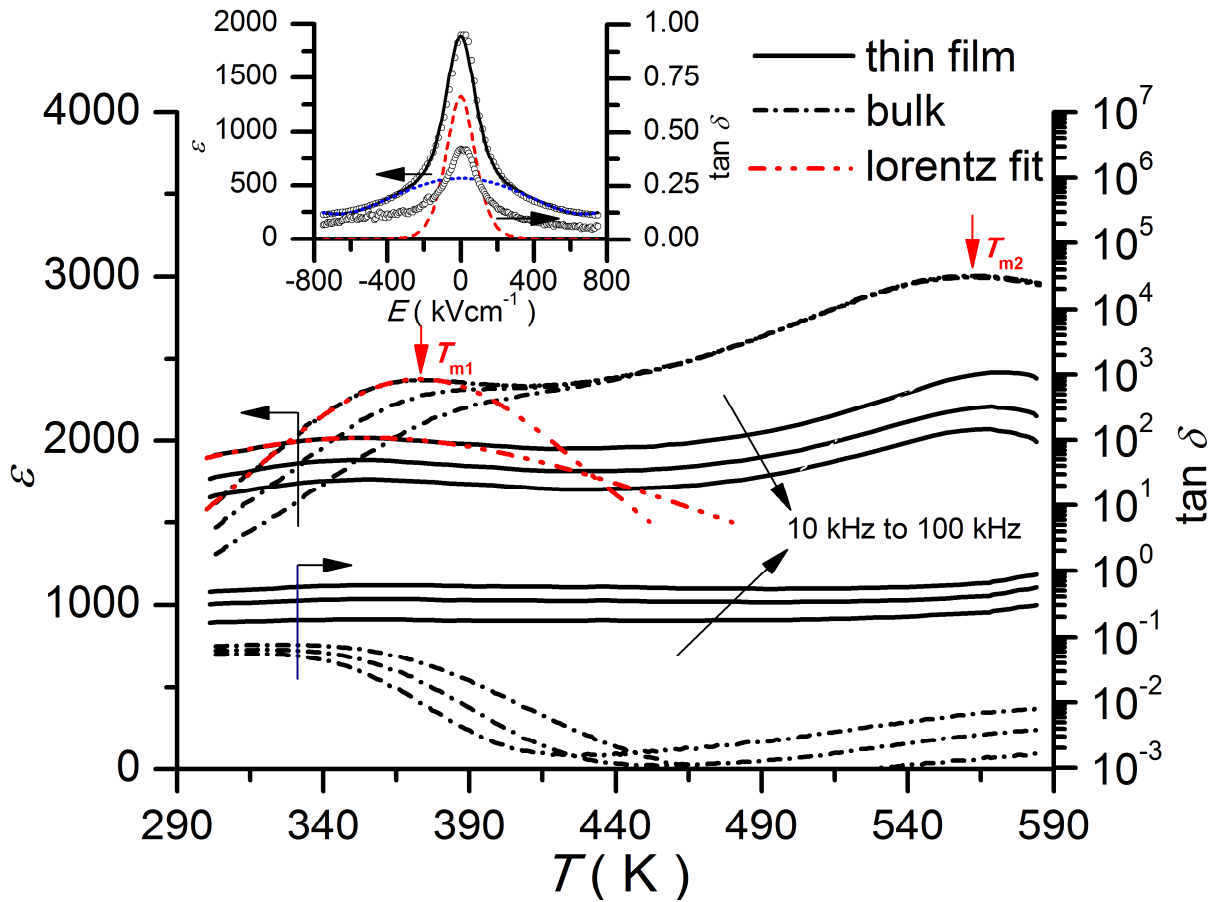


**Figure 3.**  $\varepsilon(T)$  and  $\tan \delta(T)$  of BNLBTZ bulk ceramic and (100)-oriented thin film. The inset is  $\varepsilon(E)$  and  $\tan \delta(E)$  at room temperature and 10 kHz, where the symbols represent experimental data, the black solid line is the fitting curve according to Eq. (1), the red short dashed line is the contribution from polar nanoclusters, and the blue dotted line is the contribution from lattice phonons.

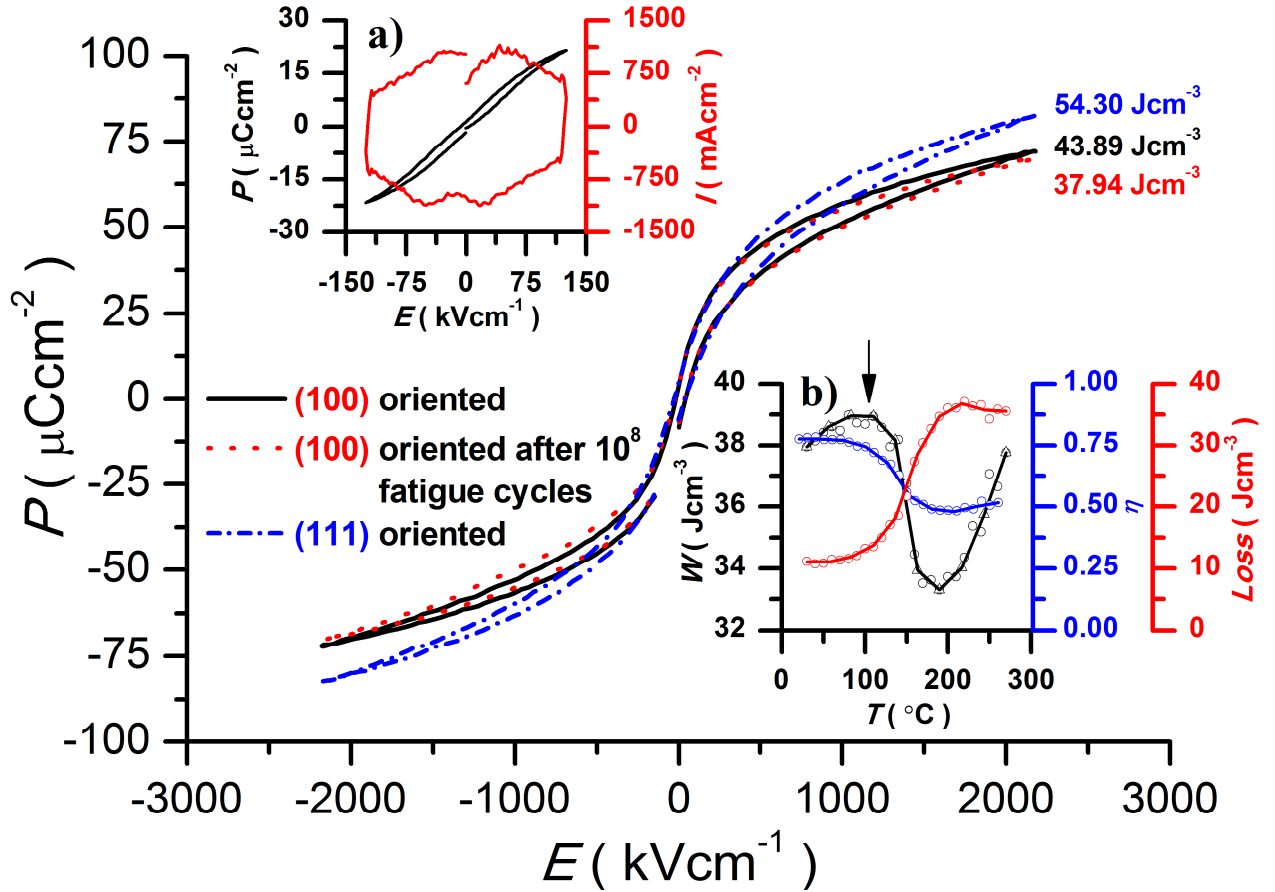


**Figure 4.**  $P$ - $E$  loops of (100)-oriented (including the one after  $10^8$  fatigue cycles) and (111)-oriented BNLBTZ thin films at room temperature and 10 kHz. The inset (a) is a typical  $P$ - $E$  loop and the corresponding  $I$ - $E$  curve of the (100)-oriented film and the inset (b) is the temperature dependence of  $W$ ,  $\eta$  and  $W_{\text{loss}}$  of the (100)-oriented film after  $10^8$  fatigue cycles.

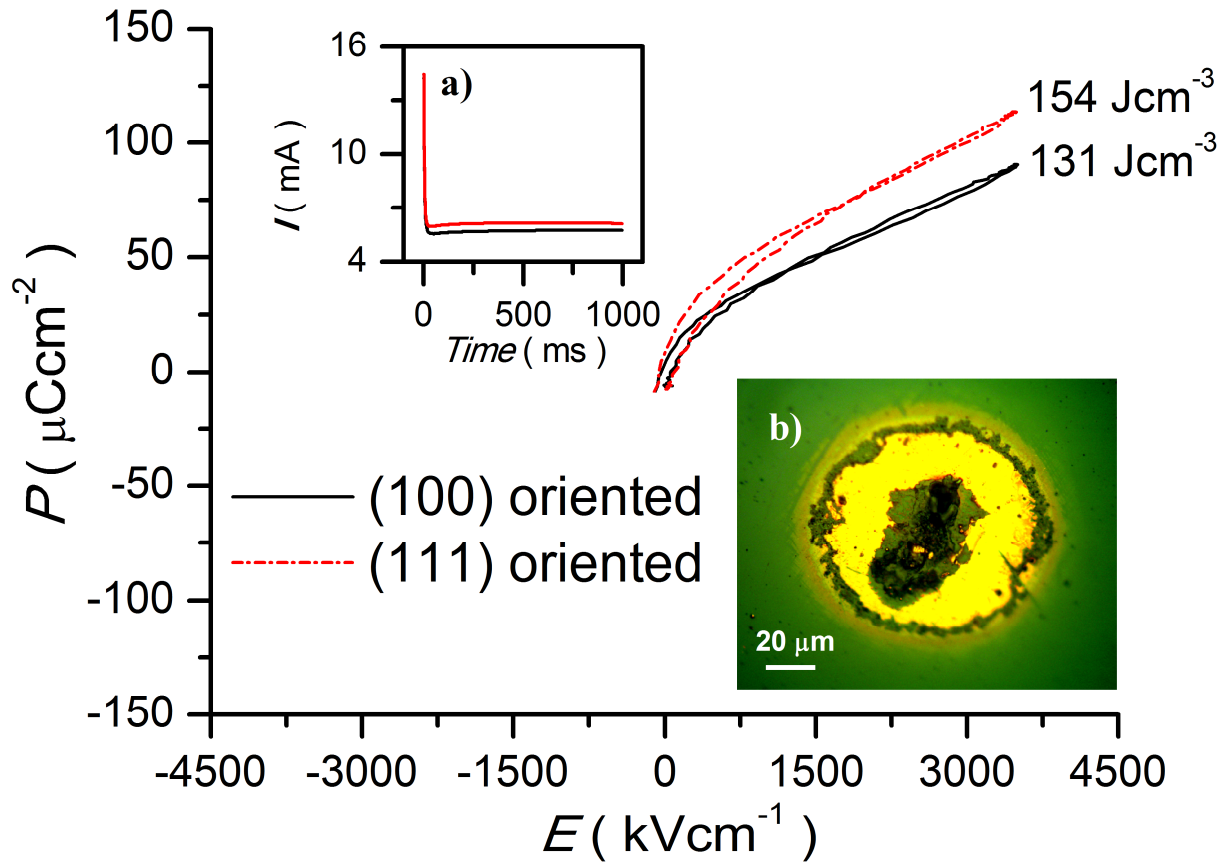


**Figure 5.**  $P$ - $E$  loops of (100)- and (111)-oriented BNLBTZ thin films at  $3500 \text{ kVcm}^{-1}$  (close to the breakdown electric field of the thin film) and  $10 \text{ kHz}$ . The inset (a) is leakage current at  $3500 \text{ kVcm}^{-1}$ , and inset (b) is the optical image of a broken electrode.

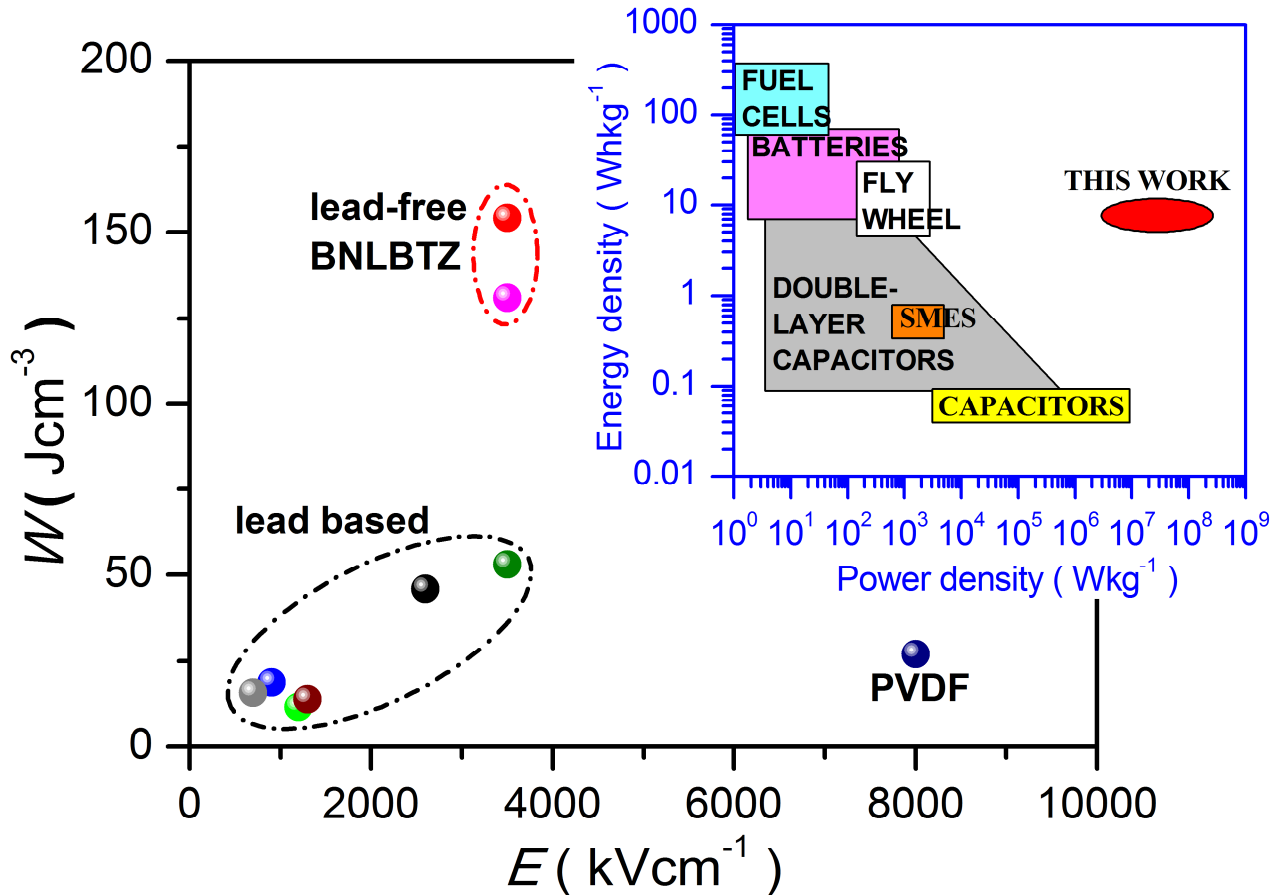


**Figure 6.** Ragone plot of the lead-free BNLBTZ thin films reported in this work and a number of lead-based FE/AFE thin and thick films, as well as polymeric PVDF. The red and the magenta dots are the (111)- and (100)-oriented BNLBTZ epitaxial thin films, respectively. The olive dot: ref.<sup>[8]</sup> the black dot: ref.<sup>[9]</sup> the blue dot: ref.<sup>[6]</sup> the wine dot: ref.<sup>[4]</sup> the gray dot: ref.<sup>[4]</sup> the green dot: ref.<sup>[12]</sup> the navy dot: ref.<sup>[4]</sup> The inset shows the Ragone plot comparing this work with some alternative storage techniques. SMES: Superconducting Magnetic Energy Storage.<sup>[4,5]</sup>

TOC:

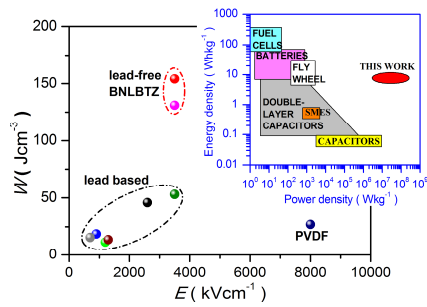
**Giant** energy density of 7.7 Wh/kg ( $154 \text{ J/cm}^3$ ) is realized in high quality doped BNT-BT epitaxial thin films, owing to the coexistence of ferroelectric and antiferroelectric phases. Both the energy density and efficiency are comparable to good electrochemical supercapacitors, leading to a bright future for the lead-free nonlinear dielectric capacitors.

**Keyword:** energy storage, relaxor, antiferroelectric, PLD, MPB

Biaolin Peng, Qi Zhang, Xing Li, Tieyu Sun, Huiqing Fan, Shanming Ke, Mao Ye, Yu Wang,

Wei Lu, Hanben Niu, James F. Scott, Xierong Zeng\*, Haitao Huang\*

### Giant Electric Energy Density in Epitaxial Lead-Free Thin Films with Coexistence of Ferroelectrics and Antiferroelectrics





Supporting Information

## **Giant Electric Energy Density in Epitaxial Lead-Free Thin Films with Coexistence of Ferroelectrics and Antiferroelectrics**

Biaolin Peng, Qi Zhang, Xing Li, Tieyu Sun, Huiqing Fan, Shanming Ke, Mao Ye, Yu Wang,  
Wei Lu, Hanben Niu, James F. Scott, Xierong Zeng\*, Haitao Huang\*

Dr. Biaolin Peng, Xing Li, Dr. Tieyu Sun, Prof. Yu Wang, Dr Wei Lu, Prof. Haitao Huang  
Department of Applied Physics, The Hong Kong Polytechnic University, Kowloon, Hong  
Kong, China  
E-mail: aphhuang@polyu.edu.hk

Dr. Biaolin Peng, Dr. Shanming Ke, Dr. Mao Ye, Prof. Xierong Zeng  
Shenzhen Key Laboratory of Special Functional Materials, Shenzhen Engineering Laboratory  
for Advanced Technology of Ceramics, College of Materials Science and Engineering,  
Shenzhen University, Shenzhen 518060, PR China.  
E-mail: zengxier@szu.edu.cn

Dr. Biaolin Peng, Prof. Hanben Niu  
Key Laboratory of Optoelectronic Devices and Systems of Ministry of Education and  
Guangdong Province, College of Optoelectronic Engineering, Shenzhen University, Shenzhen,  
518060, China.

Prof. Qi Zhang  
Department of Manufacturing and Materials, Cranfield University, Cranfield, Bedfordshire,  
MK43 0AL, United Kingdom  
State Key Laboratory of Advanced Technology for Materials Synthesis and Processing,  
Wuhan University of Technology, Wuhan 430070, Hubei, PR China

Prof. Huiqing Fan  
State Key Laboratory of Solidification Processing School of Materials Science and  
Engineering, Northwestern Polytechnical University, Xi'an 710072, China

Prof. James F. Scott  
Cavendish Laboratory, University of Cambridge, Cambridge, CB3 0HE, United Kingdom

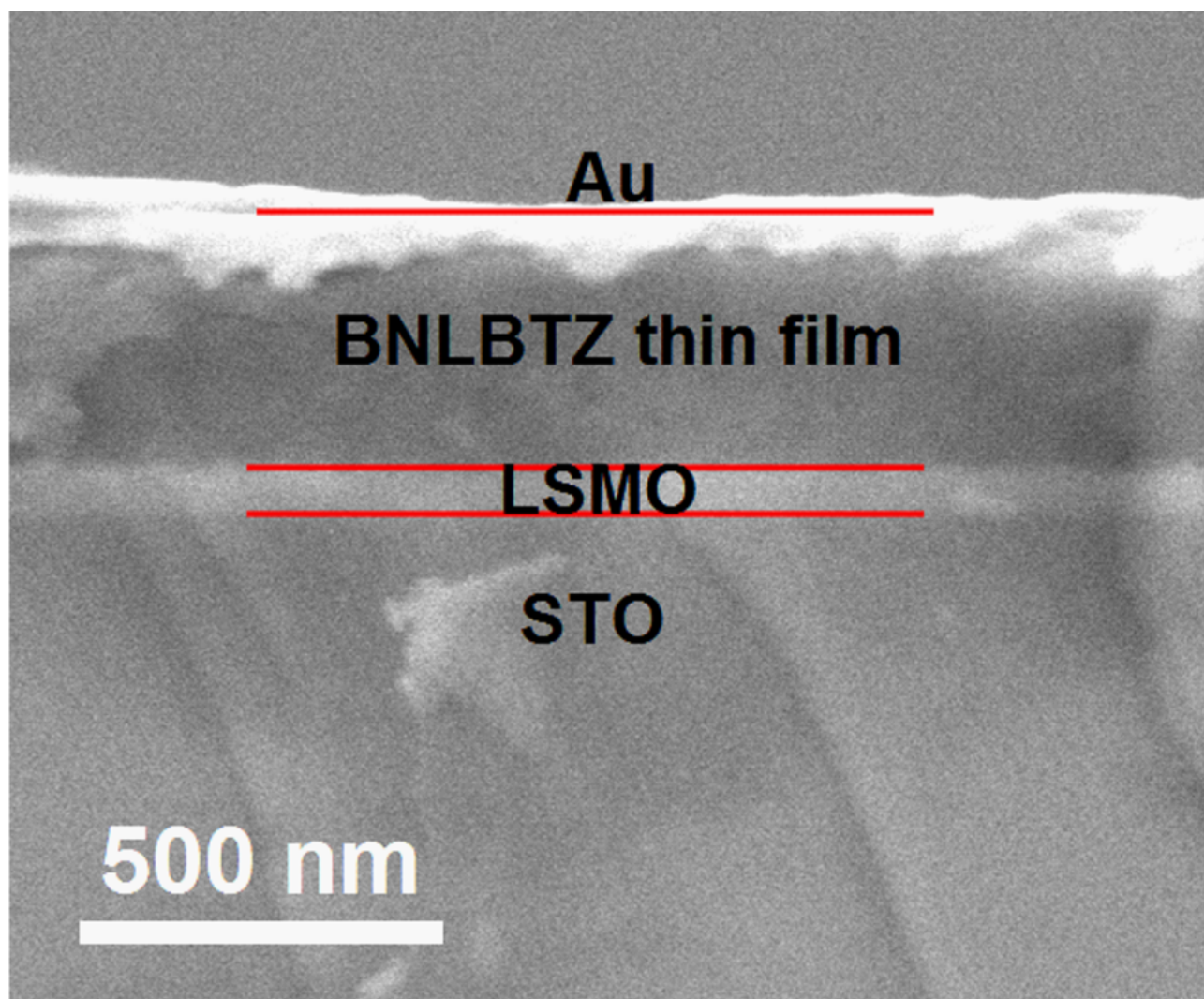


**Figure S1.** Cross-sectional SEM image of the (100)-oriented BNLBTZ thin film.

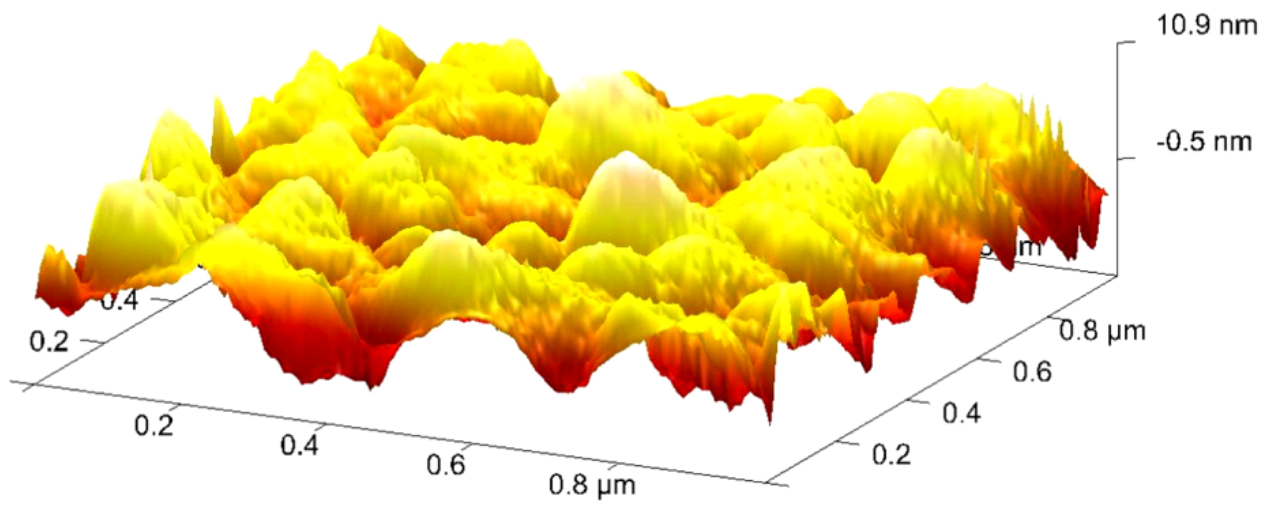


**Figure S2.** AFM micrograph of the (100)-oriented BNLBTZ thin film. The average surface roughness of Ra and Rb is about 6.3 nm and 7.9 nm, respectively.

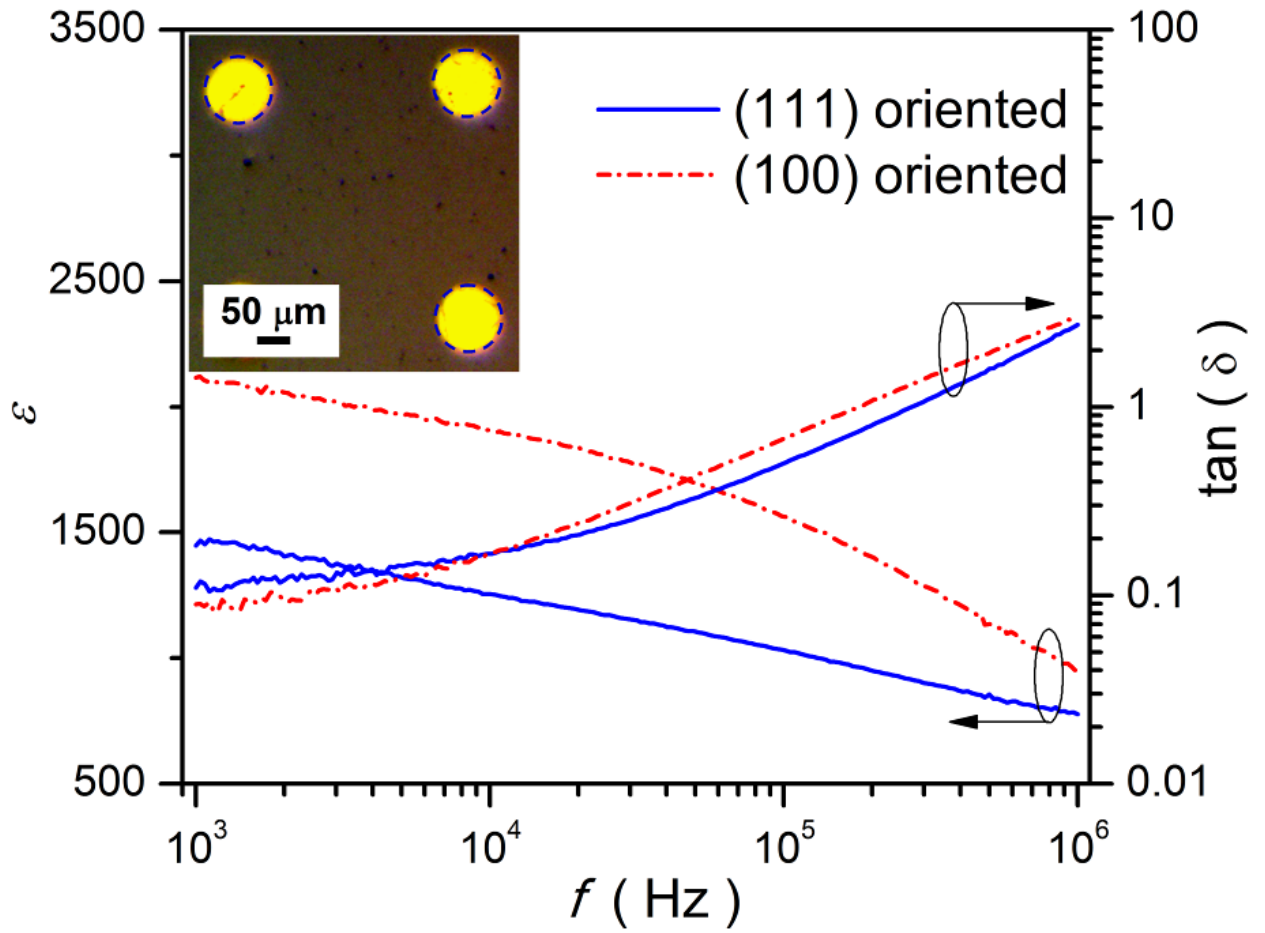


**Figure S3.** Dielectric permittivity and dielectric loss of (100)- and (111)-oriented BNLBTZ thin film at room temperature. The inset is the image of top electrodes of (111)-oriented thin film.

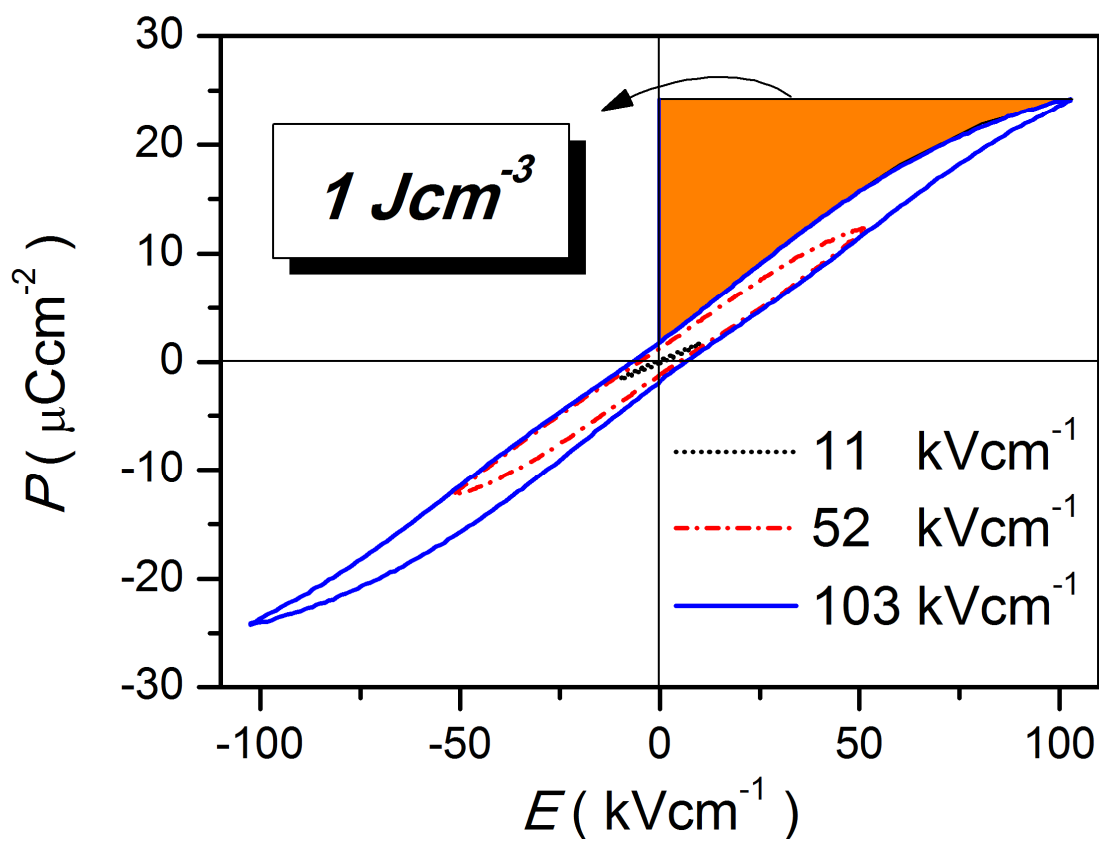


**Figure S4.**  $P$ - $E$  loops of BNLBTZ bulk ceramic at selected electric fields. The shaded area represents  $1 \text{ Jm}^{-3}$  being stored at  $103 \text{ kVcm}^{-1}$ , which is close to the breakdown electric field of the bulk ceramic.

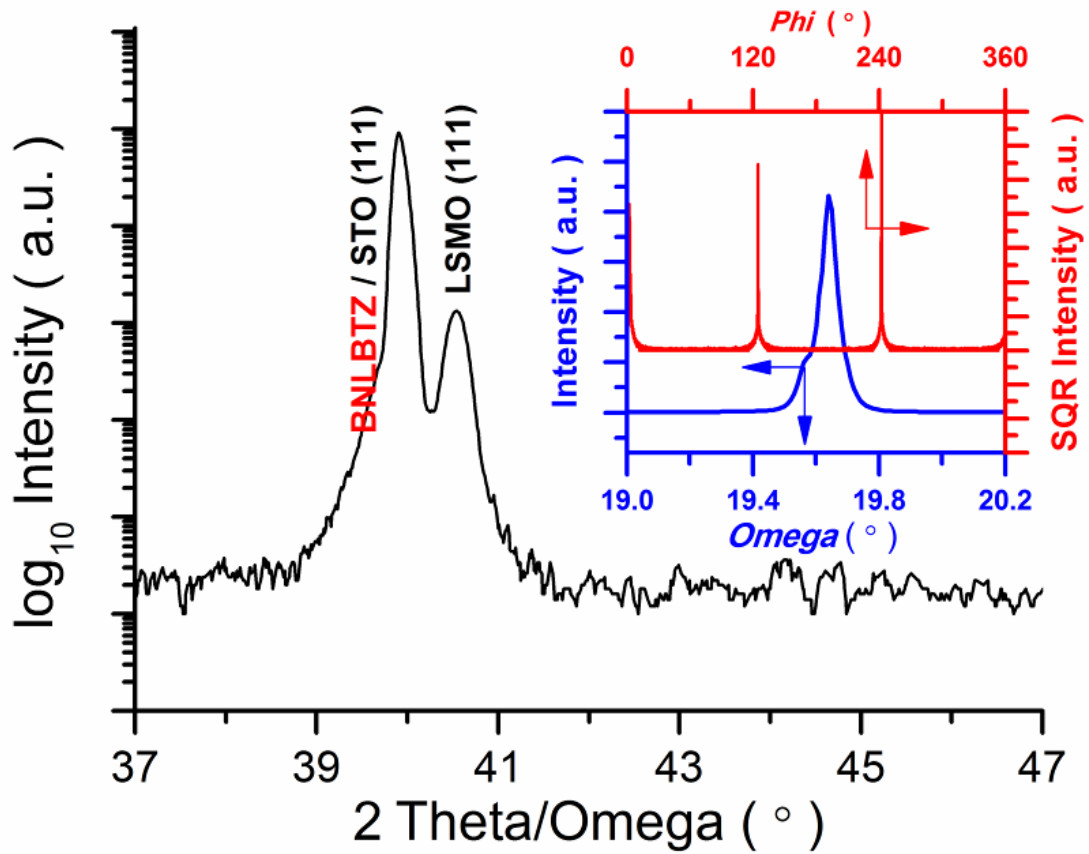


**Figure S5.** XRD pattern of (111)-oriented BNLBTZ thin film. The inset depicts the crystalline epitaxial quality (including the rocking curve of (111) and the  $\phi$  scan of (110)).

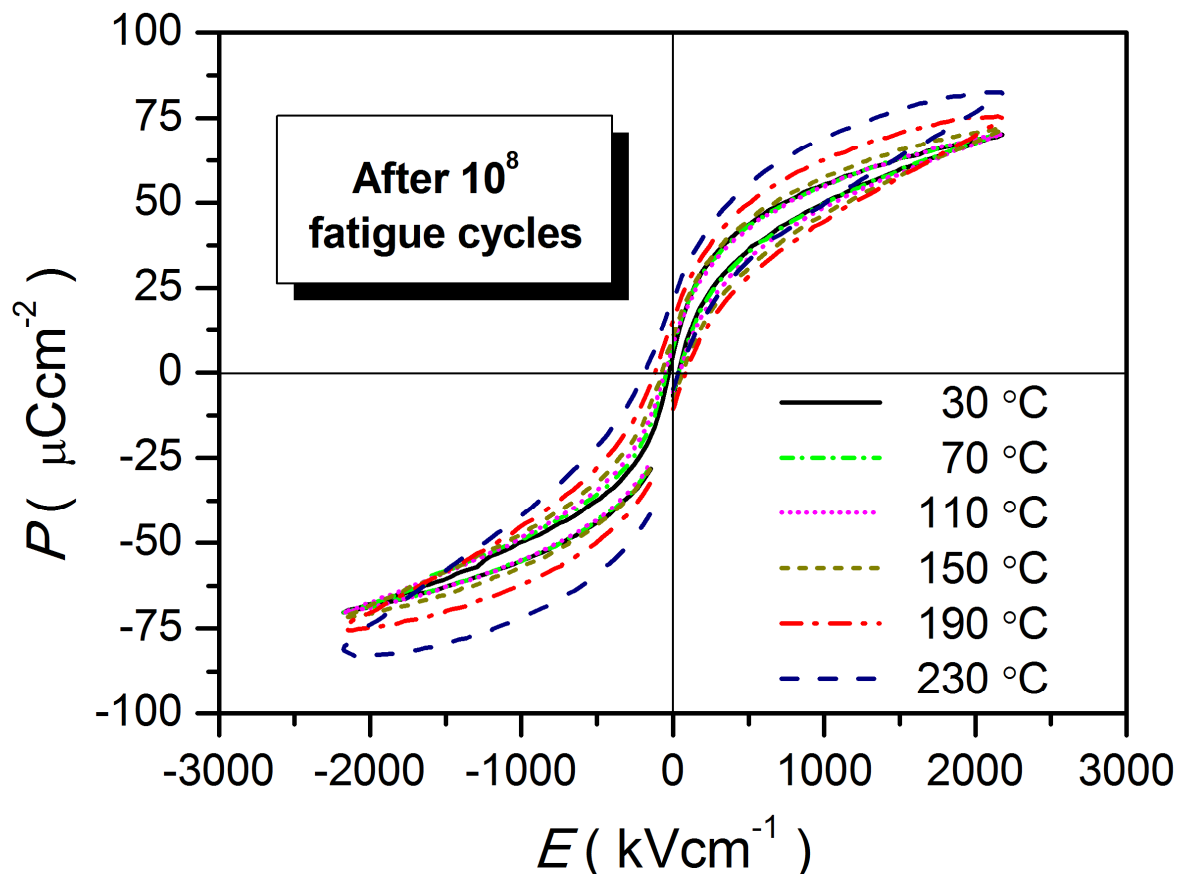


**Figure S6.** *P-E* loops of (100)-oriented BNLBTZ thin film at selected temperatures after  $10^8$  bipolar fatigue cycles.

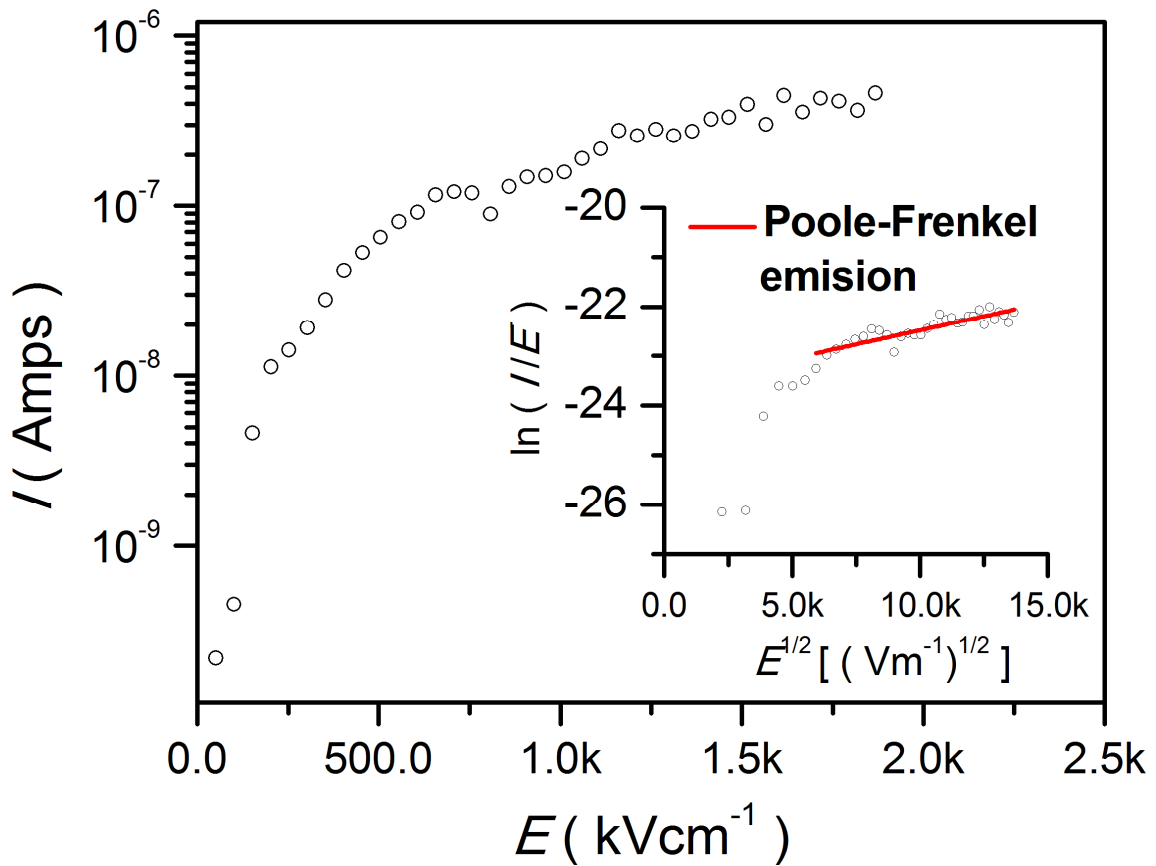


**Figure S7.** The leakage current *vs* applied electric field (*I-V*) curve for (100)-oriented BNLBTZ thin film. The  $\ln(I/E)$  is plotted as a function of  $E^{1/2}$  in the inset. The red straight line behavior at high electric field indicates Poole-Frenkel conduction mechanism.<sup>[1]</sup> The low leakage current ( $\mu\text{A}$  level) and Poole-Frenkel conduction mechanism assure the BNLBTZ epitaxial thin film a large electrical breakdown field.

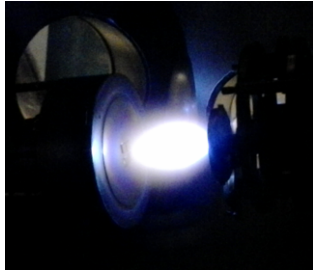


**Table S1.** Energy storage characteristics of thin films reported in this work and elsewhere.

Material	W (Jcm <sup>-3</sup> )	$\Delta E$ (kVcm <sup>-1</sup> )	W/ $\Delta E$ J/(kV·cm <sup>2</sup> )	$\eta$ (%)	Method
BNLBTZ ((100)-Oriented)	131	3500	0.037	95	PLD
BNLBTZ ((111)-Oriented)	154	3500	0.044	97	PLD
(Pb <sub>0.92</sub> La <sub>0.08</sub> )(Zr <sub>0.95</sub> Ti <sub>0.05</sub> )O <sub>3</sub> <sup>[2]</sup>	53	3500	0.0151	< 70	Sol-gel
(Pb <sub>0.92</sub> La <sub>0.08</sub> )(Zr <sub>0.52</sub> Ti <sub>0.48</sub> )O <sub>3</sub> <sup>[3]</sup>	46	2600	0.0176	< 70	Sol-gel
PbZrO <sub>3</sub> (Eu doped) <sup>[4]</sup>	18.8	900	0.0208	72	Sol-gel
(Pb <sub>0.97</sub> La <sub>0.02</sub> )(Zr <sub>0.97</sub> Ti <sub>0.03</sub> )O <sub>3</sub> <sup>[5]</sup>	11.7	1200	0.0098	< 40	Sol-gel
PZN-PMN-PT <sup>[6]</sup>	15.8	700	0.0225	< 60	Sol-gel
(Pb <sub>0.97</sub> La <sub>0.02</sub> )(Zr <sub>0.90</sub> Sn <sub>0.05</sub> Ti <sub>0.05</sub> )O <sub>3</sub> <sup>[6]</sup>	14	1300	0.0108	< 70	Sol-gel
PVDF-based <sup>[6]</sup>	27	8000	0.0033	< 40	Casting
(BiFeO <sub>3</sub> ) <sub>0.4</sub> -(SrTiO <sub>3</sub> ) <sub>0.6</sub> <sup>[7]</sup>	18.6	972	0.0191	85	PLD

**Table S2.** PLD processing parameters and corresponding plasma image.

$P_{dep}$ : oxygen pressure during deposition,  $W_{laser}$ : laser pulse energy density,  $f_{laser}$ : laser pulse frequency,  $T_{dep}$ : deposition temperature,  $T_{anneal}$ : annealing temperature,  $P_{anneal}$ : oxygen pressure during annealing.

$P_{dep}$ (Pa)	$W_{laser}$ (J/cm <sup>2</sup> )	$f_{laser}$ (Hz)	$T_{dep}$ (°C)	$T_{anneal}$ (°C)	$P_{anneal}$ (Pa)	plasma
30	5	5	700	700	400	

## Supplementary References

- [1] F.-C. Chiu, J.-J. Wang, J. Y.-m. Lee, S. C. Wu, *J. Appl. Phys.* **1997**, *81*, 6911.
- [2] B. Ma, D.-K. Kwon, M. Narayanan, U. Balachandran, *J. Mater. Res.* **2011**, *24*, 2993.
- [3] B. Ma, M. Narayanan, U. Balachandran, *Mater. Lett.* **2009**, *63*, 1353.
- [4] M. Ye, Q. Sun, X. Chen, Z. Jiang, F. Wang, R. Whatmore, *J. Am. Ceram. Soc.* **2011**, *94*, 3234.
- [5] X. Hao, J. Zhou, S. An, *J. Am. Ceram. Soc.* **2011**, *94*, 1647.
- [6] K. Yao, S. Chen, M. Rahimabady, M. S. Mirshekarloo, S. Yu, F. E. H. Tay, T. Sritharan, L. Lu, *Ieee Transactions on Ultrasonics Ferroelectrics and Frequency Control* **2011**, *58*, 1968.
- [7] T. M. Correia, M. McMillen, M. K. Rokosz, P. M. Weaver, J. M. Gregg, G. Viola, M. G. Cain, G. L. Brennecka, *J. Am. Ceram. Soc.* **2013**, *96*, 2699.